https://doi.org/10.5194/egusphere-2026-2076
Preprint. Discussion started: 15 July 2026

Slope-Constrained Orography (SCO v1.0) for explicit discrete-slope control in terrain preprocessing: a case study with WRF-ARW (v4.6.1)

Yulong Ma[1], Xingwen Jiang[2,3], Lin Mu[1], and Zhiwei Heng[2,3]

[1]College of Life Sciences and Oceanography, Shenzhen University, Shenzhen, 518055, China
[2]Heavy Rain and Drought-Flood Disasters in Plateau and Basin Key Laboratory of Sichuan Province, Institute of Tibetan Plateau Meteorology, China Meteorological Administration, Chengdu, 610072, China
[3]Institute of Tibetan Plateau Meteorology, Chinese Academy of Meteorological Sciences, Beijing, 100081, China

Correspondence: Xingwen Jiang (jiangxingwen@cma.gov.cn) and Lin Mu (mulin@szu.edu.cn)

Abstract. Kilometre-scale Weather Research and Forecasting (WRF) simulations over terrain with steep slopes often require strong smoothing to prevent numerical instability, but conventional domain-wide filters alter terrain at every grid point, regardless of whether local slopes require reduction. Slope-Constrained Orography (SCO) is an offline terrain preprocessing method that prescribes a target slope angle θ and adjusts only those grid points whose eight-neighbour elevation differences exceed the implied bound, leaving the remaining terrain unchanged while permitting stable numerical integration. By prescribing the slope constraint directly, SCO replaces the trial-and-error of filter-based smoothing with a single, geometrically interpretable control parameter. In a 1 km WRF case over the highly complex terrain of the southeastern Tibetan Plateau, the least-modified stable SCO member modifies 14 % of points with a mean elevation change of 8.2 m, compared with 100 % modification and 108.1 m for the corresponding WRF Preprocessing System (WPS) member. The stable SCO member produces lower near-surface wind and temperature errors in this case, consistent with improved terrain representation.

1 Introduction

Complex terrain exerts strong control on boundary-layer flow, thermally driven circulations, and orographic precipitation (Raderschall et al., 2008; Cannon et al., 2017; Díaz-Fernández et al., 2025), motivating the use of kilometre-scale grids to resolve ridge–valley structure. In terrain-following coordinate models such as the Weather Research and Forecasting model (WRF; Skamarock et al., 2019), the large elevation differences that arise on kilometre-scale grids over complex terrain amplify horizontal pressure-gradient errors and can trigger numerical instability within a few time steps (Mahrer, 1984; Klemp et al., 2003; Zängl et al., 2004). Terrain preprocessing is therefore necessary, but the smoothing required to prevent instability routinely modifies terrain well beyond the grid points that actually govern stability.

In the standard WRF Preprocessing System (WPS) workflow, `geogrid` applies a single pass of `smth-desmth_special` smoothing to the terrain field across the entire domain. Over steep terrain at kilometre-scale grid spacing, one pass is often insufficient, and users must increase the pass count, an integer parameter with no direct geometric correspondence to the resulting slope field. The maximum discrete slope that emerges depends on the raw terrain, the grid spacing, and the number of

https://doi.org/10.5194/egusphere-2026-2076
Preprint. Discussion started: 15 July 2026

passes, and can only be diagnosed after the smoothing is complete. Because the filter updates every grid point at each iteration, terrain changes propagate far from the locations that control stability. Successive iterations yield diminishing reductions in peak slope, and stability can only be verified by completing a trial integration.

Modifying the vertical coordinate offers an alternative path to accommodating steep slopes (Park et al., 2019; Ma and Liu, 2017), but localised terrain adjustments have also been explored within conventional preprocessing. Sheridan et al. (2023) blended lightly and heavily smoothed terrain across steep-slope regions; Raluy-López et al. (2025) applied a local Gaussian filter only to grid points exceeding a slope threshold; and Le Bouëdec et al. (2025) posed terrain adjustment as a constrained optimisation problem with prescribed slope bounds. Slope-Constrained Orography (SCO) follows a similar motivation: it prescribes a target slope angle θ as the sole control variable and adjusts only those grid points whose eight-neighbour elevation differences exceed the implied bound, leaving the rest of the terrain unchanged while maintaining stable numerical integration.

This study introduces SCO v1.0 and evaluates it against standard WPS smoothing in 1 km WRF-ARW v4.6.1 simulations over the highly complex terrain of the southeastern Tibetan Plateau. Three questions guide the evaluation: (1) can a prescribed-slope approach produce stable 48 h integrations with substantially less terrain modification than domain-wide smoothing, (2) how do the two methods differ in slope-field structure near the stability boundary, and (3) do those differences affect near-surface forecast error in this case?

2 Method and WRF implementation

2.1 Overview

SCO adjusts terrain elevation on a structured grid so that no eight-neighbour elevation difference exceeds the bound implied by a prescribed slope angle θ. For a given grid spacing, the bound follows directly from θ, so candidate terrain fields can be generated offline after `geogrid` and before `metgrid` without modifying the WRF dynamical core. Water bodies and lateral boundaries remain fixed throughout. The idealised example in Fig. 1 illustrates the basic contrast: SCO modifies only the cones whose slopes violate the bound, whereas WPS smoothing alters all four.

The adjustment proceeds through weighted pairwise projection. Whenever the elevation difference across a neighbour pair exceeds the local bound, the solver redistributes the excess between the two endpoints in proportion to their mobility weights, keeping water bodies and lateral boundaries fixed. It cycles through all neighbour pairs across eight directions and iterates until every constraint is satisfied within tolerance. An octagonal correction ensures directional isotropy across the eight-neighbour stencil (Appendix A1). The implementation assumes uniform grid spacing ($\Delta x = \Delta y$) and constrains elevation differences rather than curvature; curvature constraints are left as a possible extension (Sect. 5).

Because SCO operates on the standard `geo_em` files produced by `geogrid`, it integrates easily into the existing WPS pipeline between `geogrid` and `metgrid` with no modifications to the WRF source code. The Python implementation reads and writes `geo_em.d0X.nc` directly and is used here for both offline diagnostics and terrain construction. Source code, documentation, and a worked example are archived on Zenodo (see Code and data availability).

https://doi.org/10.5194/egusphere-2026-2076
Preprint. Discussion started: 15 July 2026

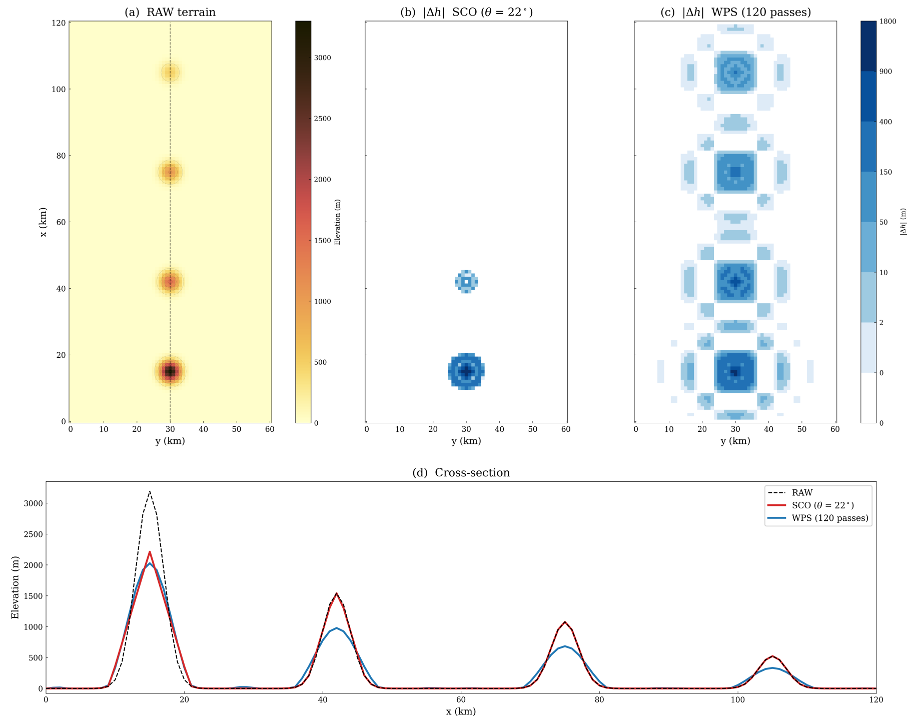

Figure 1. Idealised terrain fields used to contrast SCO and WPS smoothing. Four Gaussian cones ($\sigma = 2.0$ km) with peak slopes of 43°, 24°, 18°, and 9° are placed on a flat plain at $\Delta x = 1$ km. The effective discrete ceiling corresponding to $\theta = 22°$ is $\theta_{\text{eff}} = 20.5°$. (a) RAW terrain; the dashed line marks the cross-section in (d). (b) Absolute elevation change $|\Delta h|$ after SCO with $\theta = 22°$. (c) Absolute elevation change $|\Delta h|$ after 120 passes of WPS `smth-desmth_special`. (d) Cross-section through the cone centres.

2.2 Discrete slope metric and constraint derivation

Three slope quantities govern the constraint and its verification. The target angle θ is the user-prescribed control variable. The effective ceiling θ_{eff} is the slightly lower angle that results from enforcing an isotropic octagonal bound on the discrete eight-neighbour stencil (Appendix A1). The diagnosed maximum $S_{\text{max,int}}$ is the largest discrete slope found over the active interior after the solver converges. Their ordering is $S_{\text{max,int}} \lesssim \theta_{\text{eff}} < \theta$.

Let $h_{i,j}$ denote terrain height on a grid with spacing Δx. The local eight-neighbour discrete slope angle is

$$S_{i,j} = \max_{(m,n)\in\mathcal{N}_8(i,j)} \arctan\left(\frac{|h_{m,n} - h_{i,j}|}{d_{(i,j),(m,n)}}\right), \tag{1}$$

where $d = \Delta x$ for cardinal neighbours and $d = \sqrt{2}\,\Delta x$ for diagonal neighbours. The eight neighbours comprise the four cardinal points $(i \pm 1, j)$, $(i, j \pm 1)$ and the four diagonal points $(i \pm 1, j \pm 1)$. The maximum over active interior points (Sect. 2.3) is denoted $S_{\text{max,int}}$.

https://doi.org/10.5194/egusphere-2026-2076
Preprint. Discussion started: 15 July 2026

The constraint bound follows from requiring isotropy across the stencil. If the cardinal elevation-difference bound is set directly to $\Delta x \tan\theta$, the diagonal directions remain slightly under-constrained. The octagonal correction (Appendix A1) removes that anisotropy:

$$\Delta h^{(0)}_{\max} = \Delta x \,\tan\theta\, \cos(\pi/8). \tag{2}$$

The diagonal bound is then $\sqrt{2}\,\Delta h^{(0)}_{\max}$. Because the corrected cardinal bound is tighter than the uncorrected value, a converged solution satisfies $S_{i,j} < \theta$ everywhere in the active interior. The effective discrete ceiling is

$$\theta_{\text{eff}} = \arctan\!\big[\cos(\pi/8)\,\tan\theta\big], \tag{3}$$

and the linear approximation $\theta_{\text{eff}} \approx 0.93\,\theta$ holds to within $0.1°$ over $18°$–$26°$. The approximately 7 % gap between θ and θ_{eff} is intrinsic to the octagonal geometry: after convergence, $S_{\max,\text{int}}$ settles near θ_{eff} rather than near θ (Table 1).

2.3 Iterative projection solver

Each grid point carries a mobility weight $w_{i,j} \in [0,1]$ that controls how freely the solver may adjust its elevation. Water points receive $w = 0$ and are never modified. The outermost r rows are likewise frozen at $w = 0$; across the next t rows inward, a cosine taper raises w smoothly from 0 to 1. All remaining interior land points carry $w = 1$. The values used here are $r = 3$ and $t = 5$.

Grid points with $w > 0.5$ define the *active interior*. This threshold coincides with the midpoint of the cosine taper and marks the region over which $S_{\max,\text{int}}$ is evaluated and convergence is checked. Boundary points ($w \le 0.5$) may retain residual slope violations; these are diagnosed separately but do not enter the convergence criterion.

The solver sweeps four classes of neighbour pairs in sequence (horizontal, vertical, main diagonal, anti-diagonal) using a red–black decomposition for vectorised execution. For a pair (p,q) whose elevation difference $\delta = h_q - h_p$ exceeds the local bound L_{pq}, the excess

$$e = \delta - \operatorname{sgn}(\delta)\, L_{pq} \tag{4}$$

is redistributed according to the endpoint mobilities:

$$h_p \leftarrow h_p + e\,\frac{w_p}{w_p + w_q}, \qquad h_q \leftarrow h_q - e\,\frac{w_q}{w_p + w_q}. \tag{5}$$

When both endpoints share the same mobility the pair mean is conserved. When they differ, as in the transition zone, the more mobile endpoint absorbs the larger share and the pair mean shifts toward the less mobile point. Frozen points ($w = 0$) never move. Because each red–black subset contains only non-overlapping pairs, the maximum violation within each pair class cannot increase during a sweep.

Where steep slopes cluster, a single pass through all four pair classes can leave small residual violations. An outer loop addresses this by progressively tightening the local bound at each active interior point through a factor $f_{i,j}$, initialised to 1:

$$\Delta h_{\max,i,j} = f_{i,j}\,\Delta h^{(0)}_{\max}. \tag{6}$$

https://doi.org/10.5194/egusphere-2026-2076
Preprint. Discussion started: 15 July 2026

After each inner solve, any active interior point that still exceeds θ has its factor reduced in proportion to the overshoot:

$$f_{i,j} \leftarrow \max\left(f_{i,j}\,\beta\,\frac{\theta}{S_{i,j}},\, f_{\min}\right), \tag{7}$$

where $\beta = 0.97$ damps oscillations and $f_{\min} = 0.30$ prevents over-tightening. The outer loop terminates when $S_{\max,\text{int}} \leq \theta + 0.01°$ or after 10 iterations. Because the stopping rule references θ rather than θ_{eff}, the residual gap between $S_{\max,\text{int}}$ and θ_{eff} reflects the criterion itself rather than incomplete convergence. Each inner solve runs for at most 500 sweeps with a convergence tolerance of 0.1 m on the maximum pairwise exceedance. The full pseudocode and parameter values are given in Appendix A2. All offline diagnostics and figures in this study use `max_outer = 10`, `max_sweeps = 500`, `inner_tol = 0.1 m`, and `outer_tol_deg = 0.01°`. These are also the module defaults in the released code, which users may adjust for other domains.

2.4 Offline diagnostics

Constraint compliance is measured by $S_{\max,\text{int}}$, the maximum of $S_{i,j}$ over the active interior. The near-critical count records spatial clustering near the slope ceiling: it is the number of active interior points whose $S_{i,j}$ falls within $\varepsilon = 0.2°$ of the member's own $S_{\max,\text{int}}$. The tolerance $\varepsilon = 0.2°$ exceeds the residual convergence gap (approximately 0.01°) while remaining small enough to isolate near-ceiling clustering. A large count indicates that many grid points lie near the ceiling.

Terrain fidelity is characterised by $\text{MAE}_h = \langle |h_{\text{new}} - h_{\text{raw}}| \rangle$ over interior land points, which gives the domain-mean elevation displacement, and by the modified-area fraction, the proportion of those points where $|h_{\text{new}} - h_{\text{raw}}| > 0.1\,\text{m}$. MAE_h measures the typical magnitude of elevation change; the modified-area fraction measures how widely those changes spread. Retained short-wave terrain structure is quantified by the Laplacian RMS: the root-mean-square over interior land points of the five-point discrete Laplacian

$$L_{i,j} = h_{i+1,j} + h_{i-1,j} + h_{i,j+1} + h_{i,j-1} - 4\,h_{i,j} \tag{8}$$

(in metres). Because the Laplacian responds to second-order terrain structure, it distinguishes terrain fields with similar $S_{\max,\text{int}}$ but different short-wave content. Ridge-to-valley relief retention along cross-sections is defined as the ratio of the peak-to-valley elevation difference in the processed field to that in RAW.

3 Experimental design

3.1 Study region and model configuration

The test region is the southeastern Tibetan Plateau (Fig. 2), where raw discrete slope angles on a 1 km grid exceed 40° (Table 1). Two one-way-nested WRF-ARW v4.6.1 domains are used. The outer domain (D01) covers the eastern Tibetan Plateau margin and the Sichuan Basin on a 360×360 grid at 3 km spacing; the inner domain (D02) spans the steep plateau–basin transition on a 420×420 grid at 1 km spacing. Both domains use 54 vertical levels with a model top at 50 hPa and the hybrid terrain-following

https://doi.org/10.5194/egusphere-2026-2076
Preprint. Discussion started: 15 July 2026

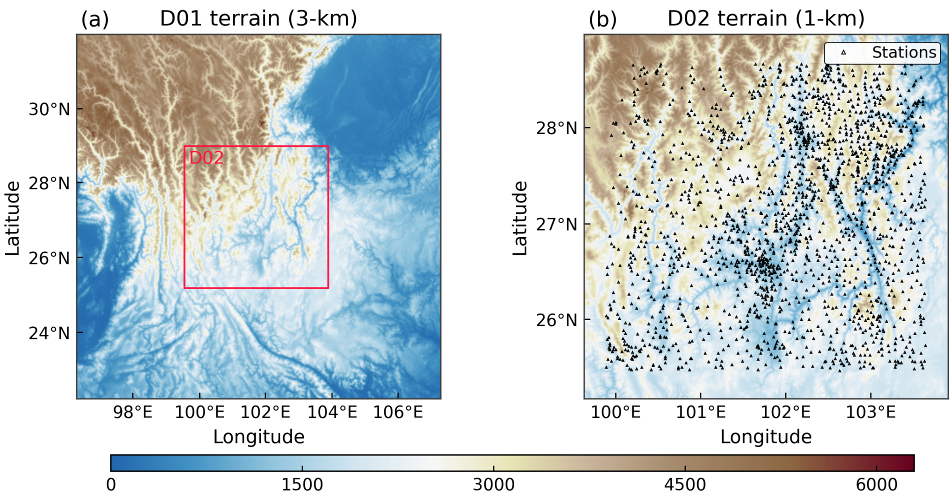

Figure 2. Model domains and observation network. (a) D01 terrain elevation (3 km grid spacing) with the D02 boundary marked. (b) D02 terrain elevation (1 km grid spacing) with the 927 surface stations used for near-surface verification.

coordinate. The time step is 18 s for D01 and 6 s for D02 for most members, reduced to 12–15 s on D01 for the more heavily smoothed WPS members to maintain numerical stability.

All simulations are initialised at 0000 UTC 18 July 2025 from ERA5 reanalysis (Hersbach et al., 2020) and integrated for 48 h. Static terrain for the 1 km inner domain is built from the 30 m ASTER Global Digital Elevation Model (GDEM; Tachikawa et al., 2011) by area averaging onto the model grid. The physics configuration is identical across all experiments: Thompson microphysics (Thompson et al., 2008), Rapid Radiative Transfer Model for GCMs (RRTMG) radiation (Iacono et al., 2008), the Yonsei University (YSU) planetary boundary layer scheme (Hong et al., 2006), the revised Fifth-Generation Penn State/NCAR Mesoscale Model (MM5) Monin–Obukhov surface layer, Noah-MP land surface model (Niu et al., 2011), and gravity-wave drag on D01 only. No cumulus parameterisation is used on either domain. The full namelist is provided in the code repository.

3.2 Terrain members and member selection

D01 terrain is fixed after a single WPS `smth-desmth_special` pass; all terrain differences among members are confined to D02. For the WPS pathway, `smth-desmth_special` is applied for N passes to the aggregated D02 terrain, and the member label gives the pass count. Five members are tested: WPS01, WPS60, WPS100, WPS120, and WPS150.

SCO members are generated by applying the slope-constrained adjustment (Sect. 2.3) directly to the unsmoothed D02 terrain. Five members span $\theta = 18°$ to $26°$ at $2°$ intervals, with the member label giving the target angle. All SCO members share the same solver settings ($r = 3$, $t = 5$, $\beta = 0.97$, $f_{\min} = 0.30$); only θ varies. RAW is retained as an offline reference. A

https://doi.org/10.5194/egusphere-2026-2076
Preprint. Discussion started: 15 July 2026

Table 1. Terrain members with offline diagnostics and stability outcomes. The control parameter is the WPS pass count N or the SCO target angle θ. For SCO members, θ_{eff} is the effective discrete ceiling under the octagonal correction (Sect. 2.2). "48 h" indicates whether the member completes the full 48 h integration; all failed members terminate within the first 15 min. W1+SCO24 MAE_h is measured relative to its WPS01-smoothed input rather than to RAW, and its modified-area fraction is not directly comparable to the RAW-referenced values of the other members; neither quantity enters the cross-method comparison.

Member	Path	Control	θ_{eff} (°)	$S_{\mathrm{max,int}}$ (°)	MAE_h (m)	Mod. (%)	48 h
RAW	–	–	–	47.73	0	0	–
WPS01	WPS	$N = 1$	–	41.49	30.4	>99.9	fail
WPS60	WPS	$N = 60$	–	26.24	96.4	>99.9	fail
WPS100	WPS	$N = 100$	–	24.44	105	>99.9	fail
WPS120	WPS	$N = 120$	–	24.13	108.1	100.0	pass
WPS150	WPS	$N = 150$	–	23.76	111.9	100.0	pass
SCO18	SCO	$\theta = 18°$	16.7	17.24	17.9	26.0	pass
SCO20	SCO	$\theta = 20°$	18.6	19.31	12.3	19.4	pass
SCO22	SCO	$\theta = 22°$	20.5	21.12	8.2	14.0	pass
SCO24	SCO	$\theta = 24°$	22.4	22.36	5.3	9.9	fail
SCO26	SCO	$\theta = 26°$	24.3	24.26	3.3	6.5	fail
W1+SCO24	Combo	$N = 1$+$\theta = 24°$	22.4	22.36	2.2 [b]	n.a. [b]	fail

[a] WPS100 MAE_h is rounded to the nearest integer. [b] W1+SCO24 MAE_h is measured relative to its WPS01-smoothed input, not relative to RAW; excluded from the cross-method comparison.

control experiment, W1+SCO24, applies one WPS pass before SCO at $\theta = 24°$ to test whether light pre-smoothing changes the stability outcome at fixed $S_{\mathrm{max,int}}$.

The cross-method comparison pairs the least-modified stable member from each method under the same 48 h stability criterion. Members are not matched by slope or terrain cost, since neither method offers a natural counterpart at fixed values of these quantities. One additional stable member from each method enters the near-surface evaluation to gauge within-method sensitivity.

3.3 Observations and verification protocol

Near-surface verification uses hourly 10 m wind speed and 2 m temperature from 927 China Meteorological Administration surface stations within the D02 interior (Fig. 2b). The denser local network improves spatial sampling in interior valleys, where terrain effects are expected to be strongest.

Stations within 30 grid points of the lateral boundaries are excluded to avoid relaxation-zone contamination, and each retained time series must contain at least 20 % valid observations during the 48 h window. At any given station, the terrain-height difference between members is much smaller than the model-minus-observation elevation offset, so systematic elevation

https://doi.org/10.5194/egusphere-2026-2076
Preprint. Discussion started: 15 July 2026

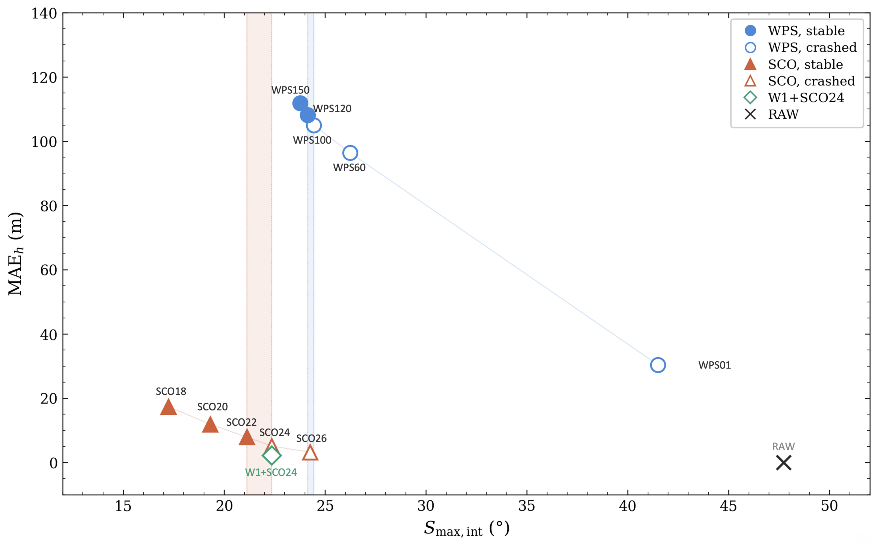

Figure 3. Terrain-member pathways in $(\mathrm{MAE}_h,\, S_{\max,\text{int}})$ space. Filled symbols indicate stable members and open symbols indicate failed members. Shaded bands mark the stability boundary intervals for each method.

bias largely cancels in the paired comparison. Model fields are bilinearly interpolated to station locations without elevation correction.

The final sample contains 44 200 wind pairs and 44 115 temperature pairs. Inter-member root-mean-square error (RMSE) differences are tested with a two-sided paired t-test across stations, each contributing one time-averaged RMSE value. The test does not account for spatial correlation among nearby stations, so the reported p values should be interpreted as approximate.

4 Results

4.1 Terrain modification and retained structure

Under the common 48 h stability criterion, SCO22 and WPS120 are the least-modified stable members for the two methods (Table 1). Their terrain costs differ by an order of magnitude. SCO22 modifies 14.0 % of interior land points with $\mathrm{MAE}_h = 8.2$ m; WPS120, which must alter the entire domain to reach a comparable stability margin, has $\mathrm{MAE}_h = 108.1$ m (Fig. 3).

SCO22 also retains far more short-wave terrain structure. Its Laplacian RMS reaches 279.8 m, nearly six times the 47.9 m of WPS120. Cross-sections confirm the same pattern: SCO22 retains 97–99 % of the RAW ridge-to-valley relief along two representative transects, compared with 79–86 % for WPS120 (Fig. 4).

All SCO members satisfy the prescribed eight-neighbour bound over the active interior, with achieved $S_{\max,\text{int}}$ settling close to θ_{eff} and remaining below θ in every case (Fig. 5). SCO24 converges cleanly yet fails within 15 min, whereas SCO22, with a

https://doi.org/10.5194/egusphere-2026-2076
Preprint. Discussion started: 15 July 2026

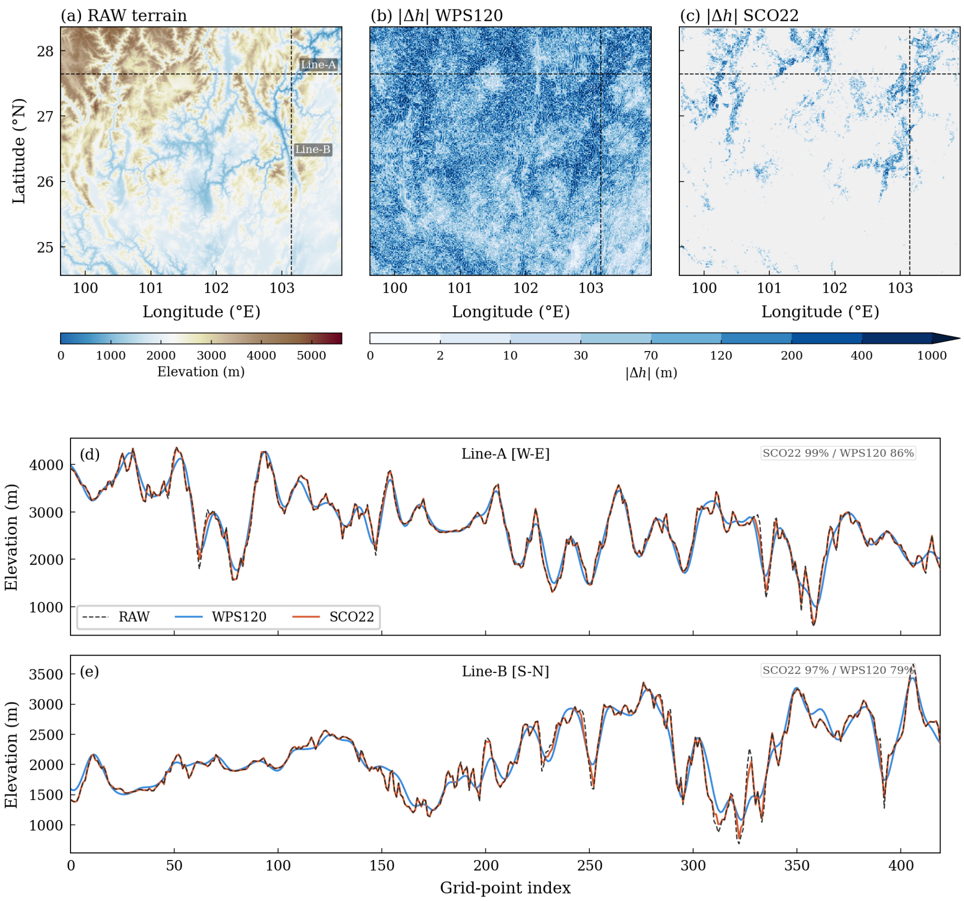

Figure 4. Terrain modification footprint and retained relief. (a) RAW terrain elevation with cross-section locations marked. (b) Absolute elevation change $|\Delta h|$ for WPS120 and (c) for SCO22, shown on the same colour scale (0–1000 m). (d) West–east cross-section A–A′ ($j = 339$) and (e) south–north cross-section B–B′ ($i = 346$). Annotated percentages denote ridge-to-valley relief retained relative to RAW.

tighter constraint, completes the full 48 h integration. Although the two members also differ in sweep count (24 vs. 10; Fig. 5b), stability is determined by the resulting terrain field rather than by the convergence behaviour.

4.2 Diagnostics near the stability boundary

Every unstable member terminates within the first 15 min with Courant–Friedrichs–Lewy (CFL) violations, indicating that the terrain field, rather than the subsequent meteorological evolution, governs the failure.

The two methods reach their stability boundaries at different $S_{\max,\mathrm{int}}$ (Table 1; Fig. 3). Along the WPS pathway, WPS100 ($S_{\max,\mathrm{int}} = 24.44°$) fails while WPS120 (24.13°) completes the full 48 h integration, placing the boundary within a 0.31° interval as sampled by the tested members. The SCO boundary is wider: SCO24 (22.36°) fails and SCO22 (21.12°) passes, a

https://doi.org/10.5194/egusphere-2026-2076
Preprint. Discussion started: 15 July 2026

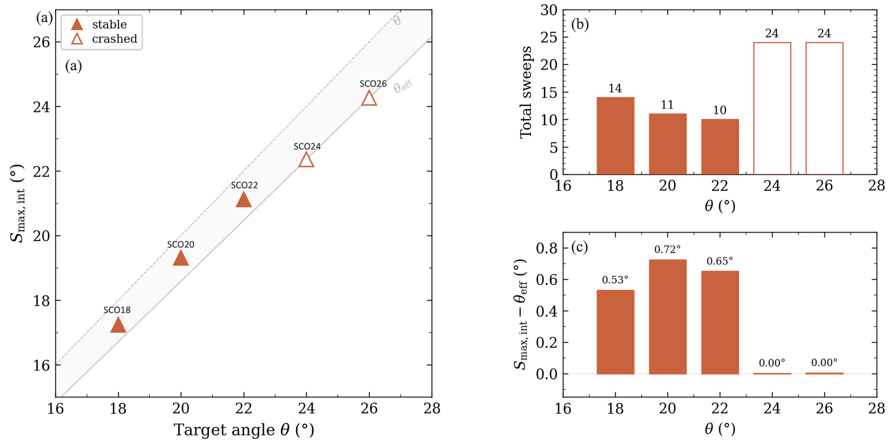

Figure 5. Target θ versus achieved $S_{\mathrm{max,int}}$ for SCO18–SCO26. (a) The dashed line marks θ_{eff}; filled triangles indicate stable members and open triangles indicate failed members. (b) Total sweep count. (c) Residual $S_{\mathrm{max,int}} - \theta_{\mathrm{eff}}$ after the final outer round.

gap of 1.24°. The two marginal stable members differ by 3.0° in peak slope, so $S_{\mathrm{max,int}}$ alone does not account for the different stability outcomes on this domain.

At the domain scale, the slope fields surrounding these boundary members differ sharply. Of the active interior points in SCO24, 15 359 fall within $\varepsilon = 0.2°$ of its own $S_{\mathrm{max,int}}$; WPS120 has only 4 (Table 2). The exceedance counts (Fig. 6b) illustrate the same contrast: SCO members drop steeply at the imposed ceiling, whereas the WPS tail decays gradually over several degrees. Because repeated smoothing progressively lowers all slopes, few WPS grid points remain near the residual peak.

In the slope probability density functions (PDFs; Fig. 6a), the contrast takes a different form: the WPS distribution falls off gradually in the upper tail, with most grid points well below the peak, while the SCO distribution is truncated sharply at the imposed ceiling and accumulates a dense population just below it. That accumulation follows from the pairwise projection, which stops adjusting each pair as soon as the bound is met.

All three failing members terminate at the same grid point on a valley-wall feature. Within a 41×41 neighbourhood centred on the failure site (Fig. 7), SCO24 retains the short-wave ridge–valley structure and brings many grid points close to the ceiling simultaneously: 604 exceed 22°. By contrast, WPS100 presents a narrow band of steep slopes against a smooth background, with only 23 grid points above 22°. The three members share the same failure location, yet the slope fields they present to the dynamical core differ considerably.

W1+SCO24 tests whether removing short-wave terrain structure at fixed $S_{\mathrm{max,int}}$ can produce a stable integration. One WPS pass applied before SCO at $\theta = 24°$ lowers the Laplacian RMS from 289.6 to 186.7 m and halves the near-critical count (from 15 359 to 7 681) while holding $S_{\mathrm{max,int}}$ at 22.36° (Table 2). Row-mean spectra confirm that about 70 % of the power near 2 km wavelength is removed, while the 10 km band remains largely intact (Fig. 8). Yet the member still fails within 15 min. Reducing curvature and spectral content without lowering $S_{\mathrm{max,int}}$ does not produce a stable integration in this case.

https://doi.org/10.5194/egusphere-2026-2076
Preprint. Discussion started: 15 July 2026

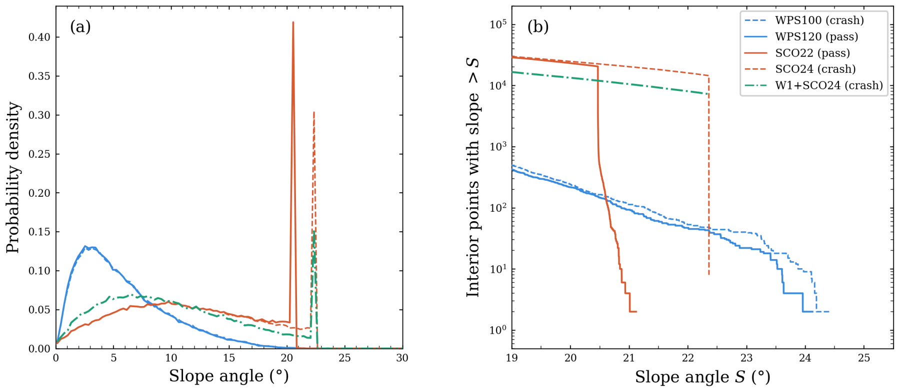

Figure 6. Slope distributions for members near the stability boundary. (a) Probability density functions for WPS100, WPS120, SCO22, SCO24, and W1+SCO24. (b) Exceedance counts: number of active interior grid points with discrete slope exceeding S, shown on a logarithmic vertical axis. The sharp drop-off in the SCO members reflects the imposed slope ceiling; the gradual tail in the WPS members reflects the progressive nature of domain-wide smoothing.

Table 2. Diagnostics for selected members near the stability boundary. Near-critical count is the number of active interior points within $\varepsilon = 0.2°$ of each member's own $S_{\mathrm{max,int}}$. Spectral retention is defined relative to RAW at the indicated wavelengths.

Member	$S_{\mathrm{max,int}}$ (°)	Near-crit. count	Lapl. RMS (m)	2 km ret. (%)	10 km ret. (%)	48 h
WPS100	24.44	2	49.9	27	30	fail
WPS120	24.13	4	47.9	27	25	pass
SCO22	21.12	6	279.8	88	91	pass
SCO24	22.36	15 359	289.6	91	94	fail
W1+SCO24	22.36	7 681	186.7	30	92	fail

Members with similar or even lower peak slope can thus differ widely in how densely near-ceiling slopes are packed. Whether that packing is causally responsible for the early CFL failure remains a working hypothesis (Sect. 5).

4.3 Near-surface verification

The four stable members (WPS120, WPS150, SCO20, and SCO22) are evaluated against the 927-station network over the full 48 h period (Table 3).

Comparing the two least-modified stable members, SCO22 produces lower errors for both variables: wind RMSE is lower by about 0.15 m s^{-1} with a weaker positive bias, and 2 m temperature RMSE is lower by about 0.16 K (Table 3). The 2 m temperature bias reverses sign between the two members (±0.17 K) but at this magnitude it is too small to diagnose a systematic difference.

https://doi.org/10.5194/egusphere-2026-2076
Preprint. Discussion started: 15 July 2026

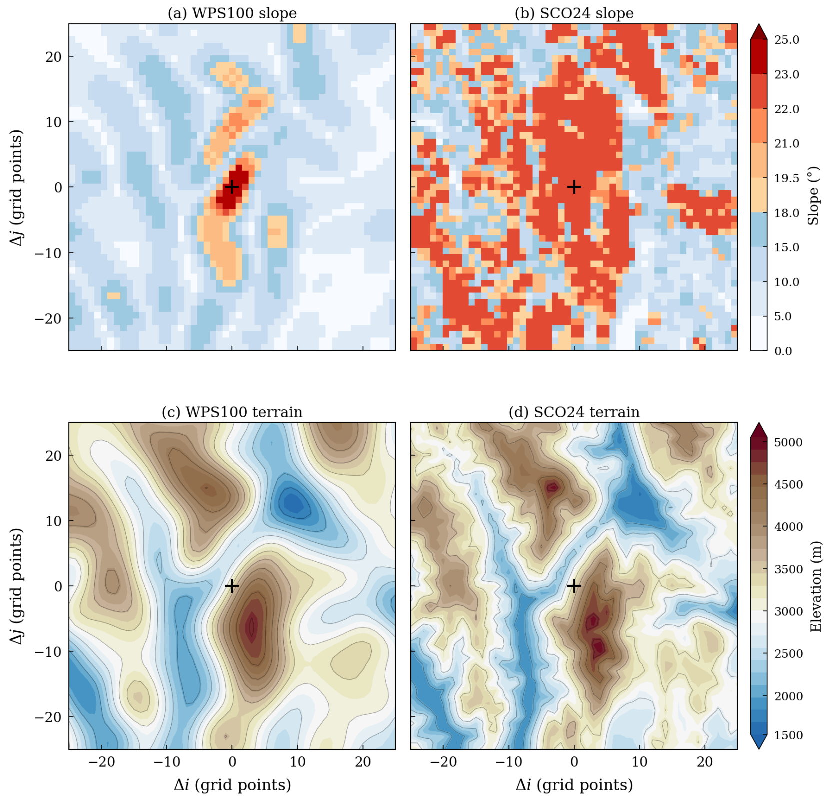

Figure 7. Local slope and elevation fields near the shared crash location (41×41 neighbourhood centred on $i = 50$, $j = 291$, 1-based). (a, b) Discrete slope $S_{i,j}$ for WPS100 and SCO24. (c, d) Terrain elevation for the same members. The cross marks the failure site.

Table 3. Forty-eight-hour near-surface verification. SCO20 and SCO22 show no detectable difference in wind RMSE ($p = 0.97$) or in 2 m temperature RMSE ($p = 0.32$) under a two-sided paired t-test across stations (Sect. 3.3).

Member	Wind RMSE ($\mathrm{m\,s^{-1}}$)	Wind bias ($\mathrm{m\,s^{-1}}$)	2 m temp. RMSE (K)	2 m temp. bias (K)
WPS120	1.790	+0.854	2.147	−0.168
WPS150	1.779	+0.844	2.194	−0.184
SCO20	1.644	+0.631	1.984	+0.164
SCO22	1.642	+0.620	1.984	+0.165

Within-method differences are much smaller. SCO20 and SCO22 are statistically indistinguishable, and the step from WPS120 to WPS150 changes scores only modestly. Because the comparison rests on a single 48 h case, these numbers are specific to the present domain and period.

https://doi.org/10.5194/egusphere-2026-2076
Preprint. Discussion started: 15 July 2026

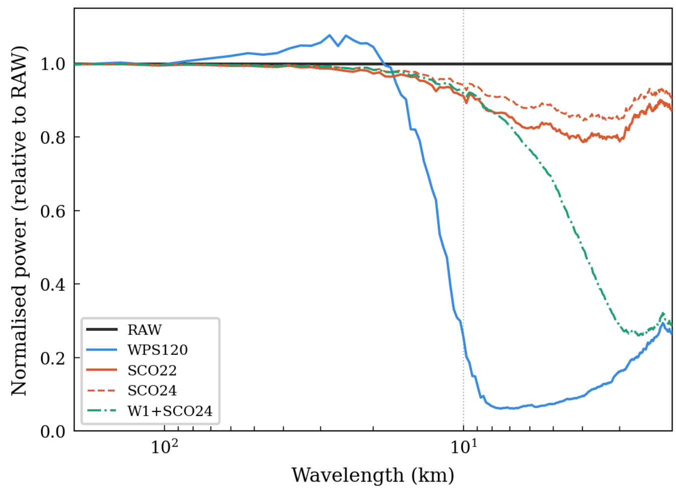

Figure 8. Normalised row-mean power spectral density for RAW, WPS120, SCO22, SCO24, and W1+SCO24. Wavelength is shown on a logarithmic horizontal axis. Vertical dotted lines mark 2 km and 10 km.

5 Discussion

SCO meets the stability criterion on this domain with far less terrain alteration than WPS, but the two methods also reach their stability boundaries at different $S_{\mathrm{max,int}}$. The spatial arrangement of near-critical slopes contributes to the boundary position alongside the peak value. WPS120 survives at a higher $S_{\mathrm{max,int}}$ than SCO24, yet the two members' slope fields differ markedly in how many grid points cluster near the ceiling. The W1+SCO24 control reinforces this interpretation: removing much of the short-wave structure while holding $S_{\mathrm{max,int}}$ fixed does not recover stability. One possible mechanism is that broad regions of near-ceiling slopes generate spatially coherent pressure-gradient truncation errors, allowing perturbations to grow before the model can dissipate them. Diagnosing the pressure-gradient tendency and vertical velocity fields during the first few time steps would test this hypothesis directly, but falls beyond the terrain-preprocessing focus of the present study. The diagnostics examined here may not capture all terrain differences relevant to stability. The two methods can produce fields that differ in ways beyond $S_{\mathrm{max,int}}$, near-critical count, and spectral content, and a much denser sampling of the stability boundary or direct diagnosis of pressure-gradient truncation error would be needed to resolve this.

The diminishing returns of repeated `smth-desmth_special` passes compound the terrain-cost asymmetry between the two methods (Fig. 3). Short-wave terrain is removed much faster than the residual peak slope declines, which explains why WPS requires such large terrain changes to reach the stability boundary. Within the stable SCO range, SCO20 and SCO22 yield nearly identical forecast scores, suggesting that once a member is well within the stable regime, further tightening of θ adds little. The practical difference between the two approaches is therefore in the stability-testing workflow itself. A filter-based approach requires the user to choose a pass count, blending factor, or filter width and then inspect the resulting slope field. SCO prescribes θ first, builds the terrain field to satisfy that bound, and uses the same variable to generate candidates, diagnose them

https://doi.org/10.5194/egusphere-2026-2076
Preprint. Discussion started: 15 July 2026

offline, test for stability, and select the final member. On the 420×420 D02 grid used here, each SCO member is generated in under 10 s on a single CPU core, so the entire five-member θ sweep completes in under a minute.

The focus of this study is not on forecast improvement through terrain modification, but on preserving terrain fidelity as far as possible while maintaining numerical stability. All terrain differences among members are confined to D02, so the interaction with the nesting configuration has not been isolated. The current implementation assumes uniform grid spacing, and extending the projection geometry to variable-resolution or unstructured meshes is a separate task.

6 Conclusions

SCO prescribes the target slope angle θ as the preprocessing control variable and enforces an eight-neighbour elevation-difference bound between `geogrid` and `metgrid`. Because θ determines the terrain field directly, SCO replaces the trial-and-error of filter-based preprocessing with a single, geometrically interpretable parameter that governs both terrain generation and stability testing. On the highly complex terrain of the southeastern Tibetan Plateau at 1 km grid spacing, the least-modified stable SCO member (SCO22) completes a 48 h integration with $\mathrm{MAE}_h = 8.2$ m and 86 % of interior land points unmodified, compared with $\mathrm{MAE}_h = 108.1$ m and 100 % modification for the least-modified stable WPS member (WPS120).

Near the stability boundary, peak slope alone does not determine stability in this case. The diagnostics suggest that the spatial density of near-ceiling slopes also plays a role in setting the boundary position, since members with comparable $S_{\mathrm{max,int}}$ produce opposite stability outcomes depending on the surrounding slope field. The mechanism remains a working hypothesis, but the contrast in near-ceiling slope density between the two methods is unambiguous.

SCO22 also produces lower near-surface wind and temperature errors in this 48 h case. Whether this advantage holds across other domains and seasons remains to be tested. Because θ controls both terrain generation and offline testing, SCO condenses the trial-and-error of filter-based preprocessing into a single parameter choice tied directly to the slope metric most relevant to stability, with each candidate terrain generated in seconds. The current implementation assumes uniform grid spacing, and extending the projection geometry to variable-resolution or unstructured meshes is a natural next step toward broader applicability.

Appendix A: Octagonal correction and algorithm summary

A1 Isotropic octagonal correction

If the cardinal elevation-difference bound is set directly to $\Delta x \tan\theta$, the eight-neighbour stencil remains rotationally anisotropic. A regular octagon inscribed in a circle of radius $\Delta x \tan\theta$ has apothem $\Delta x \tan\theta \cos(\pi/8)$. Setting the cardinal bound to this apothem gives

$$\Delta h_{\max}^{(0)} = \Delta x \tan\theta \cos(\pi/8), \quad \text{(A1)}$$

https://doi.org/10.5194/egusphere-2026-2076
Preprint. Discussion started: 15 July 2026

which places the octagonal admissible set inside the circular slope limit. The diagonal bound then becomes $\sqrt{2}\,\Delta h_{\max}^{(0)}$. This correction removes the directional bias from the target slope constraint.

260 A2 Pseudocode

The pseudocode below summarises the algorithm with the parameter values used for the terrain members analysed in this paper.

https://doi.org/10.5194/egusphere-2026-2076
Preprint. Discussion started: 15 July 2026

Algorithm A1 SCO v1.0

Input: $h(n_x, n_y)$ terrain elevation (m); $\mathrm{landmask}(n_x, n_y)$; Δx grid spacing (m); θ target slope angle (°); r, t frozen-rim and transition widths; $\beta = 0.97$, $f_{\min} = 0.30$, $\mathrm{max\_outer} = 10$, $\mathrm{max\_sweeps} = 500$, $\mathrm{inner\_tol} = 0.1$ m, $\mathrm{outer\_tol\_deg} = 0.01°$

Output: $h(n_x, n_y)$ adjusted terrain elevation

1. Compute base cardinal bound: $\Delta h^{(0)}_{\max} \leftarrow \Delta x \cdot \tan(\theta) \cdot \cos(\pi/8)$
2. Build mobility-weight field $w(n_x, n_y)$:
   - $w = 0$ where $\mathrm{landmask} < 0.5$ [water]
   - $w = 0$ in outermost r rows [frozen rim]
   - $w =$ cosine taper across next t rows [transition zone]
   - $w = 1$ elsewhere [interior land]
3. Initialise tightening factors: $f(i,j) \leftarrow 1$ for all (i,j)
4. Define active interior mask: $\mathrm{interior} \leftarrow (w > 0.5)$
5. **for** $\mathrm{round} = 1$ to $\mathrm{max\_outer}$ **do**
   - 5a. Update local bounds: $\Delta h_{\max}(i,j) \leftarrow f(i,j) \cdot \Delta h^{(0)}_{\max}$
   - 5b. **for** $\mathrm{sweep} = 1$ to $\mathrm{max\_sweeps}$ **do**
     - **for each** pair class (horiz., vert., main diag., anti-diag.) **do**
       - **for each** non-overlapping pair (p,q) **do**
         - $L_{pq} \leftarrow \min(\Delta h_{\max}(p), \Delta h_{\max}(q))$ [$\times\sqrt{2}$ for diag.]
         - $\delta \leftarrow h(q) - h(p)$
         - **if** $|\delta| > L_{pq}$ **then**
           - $e \leftarrow \delta - \mathrm{sgn}(\delta) \cdot L_{pq}$
           - $h(p) \leftarrow h(p) + e \cdot w(p)/(w(p)+w(q))$
           - $h(q) \leftarrow h(q) - e \cdot w(q)/(w(p)+w(q))$
     - Diagnose max pairwise exceedance over active pairs
     - **if** $\mathrm{max\_exceedance} < \mathrm{inner\_tol}$ **then** exit sweep loop
   - 5c. Diagnose $S_{\max,\mathrm{int}}$ from updated h over interior points
   - 5d. **if** $S_{\max,\mathrm{int}} \le \theta + \mathrm{outer\_tol\_deg}$ **then** exit outer loop
   - 5e. **for each** interior point where $S(i,j) > \theta$ **do**
     - $f(i,j) \leftarrow \max[f(i,j) \cdot \beta \cdot \theta / S(i,j),\ f_{\min}]$
6. **return** h

Boundary residuals are diagnosed separately and do not enter the outer tightening step. The octagonal correction, the mobility-weight field, the pairwise weighted projection, and the outer tightening together define the algorithm used here.

https://doi.org/10.5194/egusphere-2026-2076
Preprint. Discussion started: 15 July 2026

Code and data availability. The SCO v1.0 source code is archived on Zenodo at https://doi.org/10.5281/zenodo.19501184 (Ma, 2026) under the GNU General Public License v3.0 or later. The archive includes the reference solver (`sco_terrain.py`), the unit-test suite (`test_sco_terrain.py`), the WRF namelist (`namelist.input`), and a worked example comprising a Fig. 1 generation script (`fig1_idealized.py`), a sample `geo_em.d02.nc` file, and a driver script (`run_example.py`) that demonstrates the full offline preprocessing workflow.

The simulations were performed with the Weather Research and Forecasting Model version 4.6.1 (Skamarock et al., 2019); the exact WRF-ARW v4.6.1 source code and the WPS used for terrain preprocessing are archived on Zenodo at https://doi.org/10.5281/zenodo.20809210 (WRF Community and NCAR, 2026). ERA5 reanalysis data used for initial and boundary conditions are available from the Copernicus Climate Data Store under the Creative Commons Attribution licence: hourly data on pressure levels at https://doi.org/10.24381/cds.bd0915c6 (Hersbach et al., 2023a) and on single levels at https://doi.org/10.24381/cds.adbb2d47 (Hersbach et al., 2023b); the corresponding ERA5 domain subset is included in the reproducibility archive. The static terrain for the 1 km inner domain is the 30 m ASTER Global Digital Elevation Model version 3, distributed by the NASA LP DAAC and available at https://doi.org/10.5067/ASTER/ASTGTM.003 (NASA/METI/AIST/Japan Spacesystems and U.S./Japan ASTER Science Team, 2019); the corresponding ASTER tile subset is likewise included in the reproducibility archive.

Near-surface verification uses hourly 10 m wind speed and 2 m temperature from the China Meteorological Administration (CMA) hourly multi-element surface observation dataset (product SURF_CHN_MUL_HOR), provided by the CMA National Meteorological Information Center. These raw observations are not publicly available, but can be obtained from the CMA Meteorological Data Service Centre (https://data.cma.cn/en) on reasonable request, including for the purposes of peer review.

The reproducibility archive on Zenodo at https://doi.org/10.5281/zenodo.20809228 (Ma et al., 2026) bundles the ERA5 domain subset and ASTER tile subset noted above with everything else needed to reproduce the near-surface verification without the raw observations: the `geo_em` static-terrain fields for all members and both domains, the WPS and WRF namelists, the derived verification statistics (per-station, per-member time-averaged RMSE and bias for 10 m wind and 2 m temperature, anonymized so that no raw observation values, station coordinates, or station identifiers are included), and a reproduction script (`make_table3.py`) that regenerates the Table 3 values and the Sect. 4.3 paired *t*-tests.

Author contributions. Y. Ma designed the SCO algorithm, developed the Python implementation, carried out the offline diagnostics, and wrote the manuscript. X. Jiang configured the WRF simulations and performed the HPC integrations. L. Mu supervised the project and contributed to the experimental design. Z. Heng contributed to station-data processing and quality control. All authors reviewed and edited the manuscript.

Competing interests. The authors declare that they have no conflict of interest.

Acknowledgements. The authors thank the China Meteorological Administration for providing surface observation data.

https://doi.org/10.5194/egusphere-2026-2076
Preprint. Discussion started: 15 July 2026

295 **Financial support.** This work was supported by the National Natural Science Foundation of China (grant no. 42375160), the Guangdong Basic and Applied Basic Research Foundation (grant no. 2022A1515110841), the Shenzhen Fundamental Research Program (grant no. JCYJ20220530164400001), the Sichuan Science and Technology Program (grant no. 2024YFFK0110), and the Southwest Sichuan (Ya'an) Rainstorm Laboratory (grant no. CXNBYSYSZD202401).

https://doi.org/10.5194/egusphere-2026-2076
Preprint. Discussion started: 15 July 2026

References

Cannon, F., Carvalho, L. M. V., Jones, C., Norris, J., Bookhagen, B., and Kiladis, G. N.: Effects of topographic smoothing on the simulation of winter precipitation in High Mountain Asia, J. Geophys. Res. Atmos., 122, 1456–1474, https://doi.org/10.1002/2016JD026038, 2017.

Díaz-Fernández, J., Calvo-Sancho, C., Bolgiani, P., Sastre, M., López-Reyes, M., Fernández-González, S., and Martín, M. L.: Effect of complex orography on numerical simulations of a downburst event in Spain, Atmos. Res., 314, 107821, https://doi.org/10.1016/j.atmosres.2024.107821, 2025.

Hersbach, H., Bell, B., Berrisford, P., Hirahara, S., Horányi, A., Muñoz-Sabater, J., Nicolas, J., Peubey, C., Radu, R., Schepers, D., Simmons, A., Soci, C., Abdalla, S., Abellan, X., Balsamo, G., Bechtold, P., Biavati, G., Bidlot, J., Bonavita, M., De Chiara, G., Dahlgren, P., Dee, D., Diamantakis, M., Dragani, R., Flemming, J., Forbes, R., Fuentes, M., Geer, A., Haimberger, L., Healy, S., Hogan, R. J., Hólm, E., Janisková, M., Keeley, S., Laloyaux, P., Lopez, P., Lupu, C., Radnoti, G., de Rosnay, P., Rozum, I., Vamborg, F., Villaume, S., and Thépaut, J.-N.: The ERA5 global reanalysis, Q. J. Roy. Meteor. Soc., 146, 1999–2049, https://doi.org/10.1002/qj.3803, 2020.

Hersbach, H., Bell, B., Berrisford, P., Biavati, G., Horányi, A., Muñoz Sabater, J., Nicolas, J., Peubey, C., Radu, R., Rozum, I., Schepers, D., Simmons, A., Soci, C., Dee, D., and Thépaut, J.-N.: ERA5 hourly data on pressure levels from 1940 to present, Copernicus Climate Change Service (C3S) Climate Data Store (CDS) [data set], https://doi.org/10.24381/cds.bd0915c6, 2023a.

Hersbach, H., Bell, B., Berrisford, P., Biavati, G., Horányi, A., Muñoz Sabater, J., Nicolas, J., Peubey, C., Radu, R., Rozum, I., Schepers, D., Simmons, A., Soci, C., Dee, D., and Thépaut, J.-N.: ERA5 hourly data on single levels from 1940 to present, Copernicus Climate Change Service (C3S) Climate Data Store (CDS) [data set], https://doi.org/10.24381/cds.adbb2d47, 2023b.

Hong, S. Y., Noh, Y., and Dudhia, J.: A new vertical diffusion package with an explicit treatment of entrainment processes, Mon. Weather Rev., 134, 2318–2341, https://doi.org/10.1175/mwr3199.1, 2006.

Iacono, M. J., Delamere, J. S., Mlawer, E. J., Shephard, M. W., Clough, S. A., and Collins, W. D.: Radiative forcing by long-lived greenhouse gases: Calculations with the AER radiative transfer models, J. Geophys. Res., 113, D13103, https://doi.org/10.1029/2008JD009944, 2008.

Klemp, J. B., Skamarock, W. C., and Fuhrer, O.: Numerical consistency of metric terms in terrain-following coordinates, Mon. Weather Rev., 131, 1229–1239, https://doi.org/10.1175/1520-0493(2003)131<1229:NCOMTI>2.0.CO;2, 2003.

Le Bouëdec, E., Chemel, C., and Staquet, C.: Dealing with steep slopes when modeling stable boundary-layer flow in Alpine terrain, Q. J. Roy. Meteor. Soc., 151, e4835, https://doi.org/10.1002/qj.4835, 2025.

Ma, Y.: SCO v1.0: Slope-Constrained Orography for WRF terrain preprocessing (v1.0), Zenodo [code], https://doi.org/10.5281/zenodo.19501184, 2026.

Ma, Y., Jiang, X., Mu, L., and Heng, Z.: Reproducibility archive for "Slope-Constrained Orography (SCO v1.0) for explicit discrete-slope control in terrain preprocessing", Zenodo [data set], https://doi.org/10.5281/zenodo.20809228, 2026.

Ma, Y. and Liu, H.: Large-eddy simulations of atmospheric flows over complex terrain using the immersed-boundary method in the Weather Research and Forecasting Model, Bound.-Lay. Meteorol., 165, 421–445, https://doi.org/10.1007/s10546-017-0283-9, 2017.

Mahrer, Y.: An improved numerical approximation of the horizontal gradients in a terrain-following coordinate system, Mon. Weather Rev., 112, 918–922, https://doi.org/10.1175/1520-0493(1984)112<0918:AINAOT>2.0.CO;2, 1984.

NASA/METI/AIST/Japan Spacesystems and U.S./Japan ASTER Science Team: ASTER Global Digital Elevation Model V003, NASA EOSDIS Land Processes DAAC [data set], https://doi.org/10.5067/ASTER/ASTGTM.003, 2019.

Niu, G.-Y., Yang, Z.-L., Mitchell, K. E., Chen, F., Ek, M. B., Barlage, M., Kumar, A., Manning, K., Niyogi, D., Rosero, E., Tewari, M., and Xia, Y.: The community Noah land surface model with multiparameterization options (Noah-MP): 1. Model description and evaluation with local-scale measurements, J. Geophys. Res., 116, D12109, https://doi.org/10.1029/2010JD015139, 2011.

Park, S. H., Klemp, J. B., and Kim, J. H.: Hybrid mass coordinate in WRF-ARW and its impact on upper-level turbulence forecasting, Mon. Weather Rev., 147, 971–985, https://doi.org/10.1175/MWR-D-18-0334.1, 2019.

Raderschall, N., Lehning, M., and Schär, C.: Fine-scale modeling of the boundary layer wind field over steep topography, Water Resour. Res., 44, W09425, https://doi.org/10.1029/2007WR006544, 2008.

Raluy-López, E., Muñoz-Esparza, D., and Montávez, J. P.: A Local Terrain Smoothing Approach for Stabilizing Microscale and High-Resolution Mesoscale Simulations: a Case Study Using FastEddy® (v3.0) and WRF (v4.6.0), EGUsphere [preprint], https://doi.org/10.5194/egusphere-2025-3744, 2025.

Sheridan, P., Xu, A., Li, J., and Furtado, K.: Use of targeted orographic smoothing in very high resolution simulations of a downslope windstorm and rotor in a sub-tropical highland location, Adv. Atmos. Sci., 40, 2043–2062, https://doi.org/10.1007/s00376-023-2298-0, 2023.

Skamarock, W. C., Klemp, J. B., Dudhia, J., Gill, D. O., Liu, Z., Berner, J., Wang, W., Powers, J. G., Duda, M. G., Barker, D. M., and Huang, X.-Y.: A description of the advanced research WRF version 4, NCAR Tech. Note NCAR/TN-556+STR, https://doi.org/10.5065/1dfh-6p97, 2019.

Tachikawa, T., Hato, M., Kaku, M., and Iwasaki, A.: Characteristics of ASTER GDEM version 2, in: 2011 IEEE International Geoscience and Remote Sensing Symposium, Vancouver, BC, Canada, 3657–3660, https://doi.org/10.1109/IGARSS.2011.6050017, 2011.

Thompson, G., Field, P. R., Rasmussen, R. M., and Hall, W. D.: Explicit forecasts of winter precipitation using an improved bulk microphysics scheme. Part II: Implementation of a new snow parameterization, Mon. Weather Rev., 136, 5095–5115, https://doi.org/10.1175/2008mwr2387.1, 2008.

WRF Community and NCAR: Weather Research and Forecasting (WRF) Model and WRF Preprocessing System (WPS) (WRF-ARW v4.6.1), Zenodo [code], https://doi.org/10.5281/zenodo.20809210, 2026.

Zängl, G., Gantner, L., Hartjenstein, G., and Noppel, H.: Numerical errors above steep topography: A model intercomparison, Meteorol. Z., 13, 69–76, https://doi.org/10.1127/0941-2948/2004/0013-0069, 2004.